

Title No. 120-S66

Quasi-Static Cyclic Flexural Loading Behavior of Precast Reinforced Concrete Tunnel Segments with Glass Fiber-Reinforced Polymer Bars

by Basil Ibrahim, Salaheldin Mousa, Hamdy M. Mohamed, and Brahim Benmokrane

The strength and behavior of segments of precast concrete tunnel linings (PCTLs) reinforced internally with fiber-reinforced polymer (FRP) bars under quasi-static cyclic flexural loading is one area in which no experimental research results are available. This research investigated the cyclic behavior of glass FRP (GFRP)-reinforced PCTL segments, both experimentally and theoretically. Full-scale specimens with a total length, width, and thickness of 3100 mm (122 in.), 1500 mm (59 in.), and 250 mm (9.8 in.), respectively, were constructed and tested under quasi-static cyclic flexural loading. Two cycles of loading and unloading were applied at 1.25%, 2.5%, 5%, 10%, 25%, 50%, and 75% of the estimated maximum displacement, followed by a single cycle up to failure. The test parameters included reinforcement flexural stiffness (GFRP versus steel) and GFRP longitudinal reinforcement ratio. The hysteresis response, cracking pattern, residual deformation, dissipated energy, deformability, and secant stiffness damage index of the tested specimens were defined, estimated, and evaluated. The experimental results of this study show that the hysteresis cycles of the GFRP-reinforced specimens reflected stable cyclic behavior with no or limited strength degradation. Moreover, the test results show that the GFRP-reinforced specimens demonstrated adequate ductility index and deformability limits. A theoretical prediction according to the various current design provisions—including the flexural and shear capacities of the PCTL segments—was carried out and compared to the experimental results. The results of this study show the feasibility and efficiency of using GFRP bars instead of steel bars for PCTL segments under quasi-static cyclic flexural loading.

Keywords: deformability; design codes; energy dissipation; flexural and shear strength; glass fiber-reinforced polymer (GFRP) bars; hysteretic behavior; precast concrete tunnel lining (PCTL) segments; quasi-static cyclic load.

INTRODUCTION

The use of precast concrete tunnel lining (PCTL) systems in tunneling construction projects has been gaining ground over conventional on-site lining technique because of its economic efficiency. PCTL speeds the construction process and ensures the highest quality due to enhanced control during the fabrication of precast segments in precast plants (Cheong et al. 2005). The structural performance of PCTL segments significantly depends on their durability performance. Tunnel structures built with steel-reinforced concrete are designed for service lives exceeding 100 years. The ingress of chloride ions into PCTL segments can induce reinforcement corrosion, which has been the primary cause threatening the structural safety of PCTLs and shortening

their designed service lives. Corrosion of embedded reinforcement bars is considered the most prevalent mode of deterioration affecting the serviceability, safety, and structural integrity of tunnel structures (Gulikers 2003). In fact, many reinforced concrete (RC) tunnels around the world are deteriorating as they age (Zhiqiang and Mansoor 2013). Steel-reinforced PCTLs often experience premature degradation mainly due to corrosion of the reinforcement bars, requiring expensive repairs and maintenance. Because concrete is not perfectly impermeable, groundwater—often high in chlorine—gradually saturates the concrete, ultimately permeating the cover and producing an electrolytic reaction with the steel, which accelerates corrosion of the reinforcement (Rancourt 2016). This corrosion can lead to oxide jacking (also known as rust burst) and loss of structural integrity. Corrosion of steel reinforcement is the most expensive and problematic deterioration mechanism in concrete structures (ACI 440.1R-15 [ACI Committee 440 2015]). In Canada, the annual cost of repairing corrosion damage in reinforced concrete structures has been estimated at more than \$10 billion per year (Davis 2000). In the United States, the problem of corrosion of reinforced concrete structures costs the economy approximately \$100 billion each year, or nearly 1% of the country's gross domestic product (Whitmore and Ball 2004). One effective solution to this corrosion problem is to replace steel reinforcement with noncorroding fiber-reinforced polymer (FRP) reinforcing bars. These lightweight, high-strength FRP bars are characterized by high corrosion resistance, long service life, and reduced maintenance costs (Manalo et al. 2020).

Recently, a few studies investigated the possibility of using glass FRP (GFRP) reinforcement in PCTL segments (Caratelli et al. 2017; Spagnuolo et al. 2017; Meda et al. 2019; Hosseini et al. 2022). All these studies proved the suitability of using GFRP bars as reinforcement for PCTL segments. The experimental evidence from these investigations showed that the GFRP-reinforced PCTL segments exhibited better cracking control behavior compared to traditional reinforced concrete segments. The load related to the first crack was higher and the crack openings were

ACI Structural Journal, V. 120, No. 4, July 2023.

MS No. S-2022-029.R1, doi: 10.14359/51738719, received June 16, 2022, and reviewed under Institute publication policies. Copyright © 2023, American Concrete Institute. All rights reserved, including the making of copies unless permission is obtained from the copyright proprietors. Pertinent discussion including author's closure, if any, will be published ten months from this journal's date if the discussion is received within four months of the paper's print publication.

narrower. Moreover, these studies revealed no significant difference in the flexural behavior of the GFRP-reinforced PCTL segments compared to the steel-reinforced ones. Substantively, increasing of the strength of the GFRP bars compensated for the lack of ductility compared to the steel-reinforced PCTL segments. Past studies, however, have focused mainly on the static flexural resistance of PCTLs to evaluate their structural properties. During its service life, a tunnel structure can be subjected to permanent loads (dead loads, earth pressure, surcharge loads), live loads (vehicular loads, live-load surcharges, and so on), or transient loads (water loads, earthquake, superimposed deformations, blasts, fire, construction loads). According to ACI 544.7R-16 (ACI Committee 544 2016), the loads acting on PCTLs from the time of segment casting up to the time of segment erection within the tunnel-boring machine (TBM) shield fall into three stages. They are termed the production and transient stage, the construction stage, and the service stage. The internal forces and stresses in the production and transient stages are included in the design of PCTL segments. The construction stage includes the TBM jacking thrust loads on the circumferential ring joints and the pressures during the grouting operation exerted against the exterior of the completed rings. PCTL segments are designed to resist significant bursting and spalling tensile stresses that develop along the circumferential joints due to advancement of the TBM. The final service stages are represented by the long-term loads imposed on the lining from the ground, groundwater, surcharges, and other loads (such as seismic loads). The flexural behavior of steel-fiber reinforced concrete and conventionally steel-reinforced PCTL segments under quasi-static cyclic flexural loading was experimentally studied by Abbas (2014). It was revealed that both steel-fiber reinforced concrete and conventionally steel-reinforced PCTL segments exhibited reasonable levels of ductility and energy dissipation capacities and satisfied the flexural requirement under quasi-static cyclic flexural loading. Basically, there are no research results in the literature on the cyclic behavior of GFRP-reinforced PCTLs. Accordingly, the performance of full-scale PCTL segments under quasi-static cyclic flexural loading needs to be investigated.

This study is part of an ongoing comprehensive research program carried out in the Department of Civil Engineering at the University of Sherbrooke to improve current practices and develop more efficient design and construction approaches for using curvilinear GFRP bars and stirrups in precast concrete tunnel lining segments. Full-scale GFRP-reinforced PCTL segments are tested under different loading conditions—static flexural loading (Hosseini et al. 2022), quasi-static cyclic flexural loading, and punching shear and settlement—to investigate different variables and design parameters. This paper presents the structural behavior of full-scale GFRP-reinforced PCTL segments under quasi-static cyclic flexural loading, according to ACI 374.2R-13 (ACI Committee 374 2013). The effect of reinforcement type and ratio on the behavior of GFRP-reinforced precast concrete tunnel lining segments under quasi-static cyclic flexural loading was investigated. This paper is the first study to investigate the cyclic behavior of PCTL

segments reinforced with GFRP bars. It also aimed at determining the feasibility and efficiency of using GFRP instead of steel reinforcement.

RESEARCH SIGNIFICANCE

The design of the PCTL segments reinforced with FRP bars is not defined or discussed in the current design provisions such as in ACI 440.1R-15, ACI 544.7R-16, and ACI 533.5-20 (ACI Committee 533 2020). The strength and behavior of such members reinforced with FRP bars is one area in which limited research results are available for implementing this noncorroding composite reinforcement. So far, this research is the first experimental work aimed at providing experimental data involving the laboratory testing of the performance of PCTL segments reinforced with GFRP reinforcement under quasi-static cyclic flexural loading. Full-scale PCTL specimens were tested to determine the effects of reinforcement flexural stiffness (GFRP versus steel) and GFRP longitudinal reinforcement ratio. A theoretical study was also conducted to calculate the flexural and shear capacities of PCTL segments reinforced with GFRP bars according to the various current design provisions (ACI 440.1R-15; CSA S806-12(R2017) 2017; *fib* TG-9.3 2007; CNR-DT 203 2006; AFGC 2021). As this study presents the first results of their kind on the applicability of using GFRP as internal reinforcement for PCTLs under quasi-static cyclic flexural loading, the results reported in this manuscript represent a significant contribution to the relevant literature and provide end users, engineers, and code committees with much-needed data and recommendations to advance the use of GFRP reinforcement in PCTL segments. The study also is expected to be a step toward further research to assess the possibility of developing new applications for GFRP bars and ties, resulting in more durable, economic, and competitive PCTL segments for tunnel applications.

EXPERIMENTS

Materials

Table 1 provides the mechanical properties of the GFRP and steel bars used to reinforce the PCTL segments in this study. The GFRP bars were manufactured by pultruding boron-free glass fibers impregnated in a thermosetting vinyl-ester resin. The ultimate tensile strength f_{tu} and modulus of elasticity E_f of the GFRP bars were determined according to ASTM D7205 (2021). The GFRP bars had a sand-coated surface to enhance bonding and force transfer between the bars and concrete. Number 6 (20 mm), No. 5 (15 mm), and No. 4 (13 mm) GFRP bars were used for both longitudinal and transverse reinforcement in the segments, as shown in Figure 1(a). Moreover, No. 6 (20 mm) and No. 5 (15 mm) closed U-shaped GFRP bars were used as anchorage for the longitudinal reinforcement bars. For the control specimen, deformed 15M (16 mm) steel bars were used as longitudinal reinforcement and deformed 10M (11 mm) steel bars as transverse reinforcement. Deformed 15M (16 mm) U-shaped steel bars were used to anchor the longitudinal reinforcement bars.

All PCTL segments were cast with normalweight concrete by a local precast company. The average actual compressive

Table 1—Mechanical properties of reinforcement bars

Reinforcement type	Bar size	Bar diameter, mm	Nominal cross-sectional area, mm ²	Modulus of elasticity, GPa	Tensile strength, MPa	Tensile strain, %
Curvilinear GFRP bars	No. 5	15.0	199	55.1	1115	2.0
	No. 6	20.0	284	52.9	1068	2.0
U-shaped GFRP bars	No. 5	15.0	199	53.5	1283	2.4
	No. 6	20.0	284	53.2	1131	2.1
Closed GFRP ties	No. 4	13.0	129	55.6	1248	2.2
Steel bars	10M	11.3	100	200.0	480*	0.24 [†]
	15M	16.0	200	200.0	460*	0.23 [†]

*Yield strength of steel bars.

[†]Yield strain of steel bars.

Note: 1 mm = 0.0394 in.; 1 MPa = 145 psi; 1 GPa = 145 ksi.

Table 2—Test matrix

Specimen ID	Reinforcement type	Concrete compressive strength f'_c , MPa	Longitudinal reinforcement		Transverse reinforcement
			ρ_f , %	Number of bars	
7S15	Steel	53	0.5	Seven 15M bars	10M bars @ 200 mm
7G15	GFRP	52	0.5	Seven No. 5 bars	No. 4 bars @ 200 mm
13G15	GFRP	52	0.9	Thirteen No. 5 bars	No. 4 bars @ 200 mm
13G20	GFRP	50	1.2	Thirteen No. 6 bars	No. 4 bars @ 200 mm

Note: 1 mm = 0.0394 in.; 1 MPa = 145 psi.

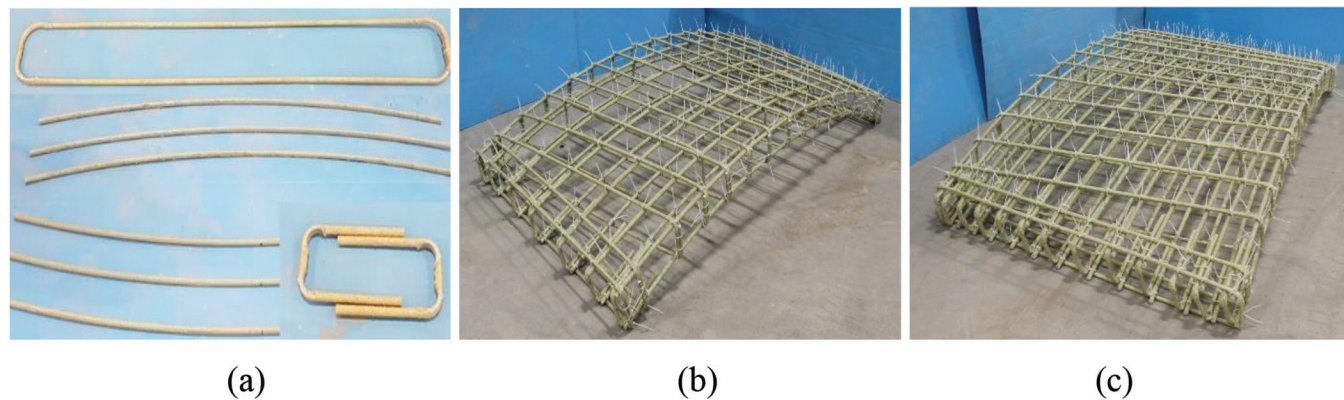


Fig. 1—Overview of: (a) GFRP bars and ties; (b) assembled GFRP cage for specimens with seven top and bottom longitudinal bars; and (c) assembled GFRP cage for the specimens with 13 top and bottom longitudinal bars.

strength based on the average test results of 100 x 200 mm (3.94 x 7.89 in.) concrete cylinders tested on the first day of the start of testing of the specimens was 52.2 MPa (7.6 ksi).

Specimen details

The experimental program was designed to provide data on the cyclic behavior of PCTL segments reinforced with GFRP bars. Four full-scale PCTL segments (three reinforced with GFRP bars and one with conventional steel reinforcement) were tested under quasi-static cyclic flexural loading. The inner and outer radii of the four PCTL segments were designed to be 3250 and 3500 mm (128 and 138 in.), respectively. The test specimens measured 3100 mm (122 in.) in length, 1500 mm (59 in.) in width, and 250 mm (9.8 in.) in thickness. The segments were skewed at their ends rather than straight. Figures 1(b) and (c) show assembled GFRP

cages for the test specimens. The test matrix was arranged to assess the influence of the flexural reinforcement type (GFRP versus steel) and the GFRP flexural reinforcement ratio. Longitudinal reinforcement ratios of 0.5%, 0.9%, and 1.2% were chosen as the minimum reinforcement ratio for concrete crushing controlled by flexural failure, an intermediate reinforcement ratio, and the maximum reinforcement ratio practically possible. Table 2 provides the test matrix and reinforcement details of the test specimens. The test specimens are identified as follows. The first number indicates the number of longitudinal bars. The letters G and S stand for GFRP and steel reinforcement, respectively. The second number indicates the nominal diameter of the longitudinal bars. Specimen 7G15 had top and bottom longitudinal reinforcement consisting of seven No. 5 GFRP bars with a longitudinal reinforcement ratio of 0.5%. Seven

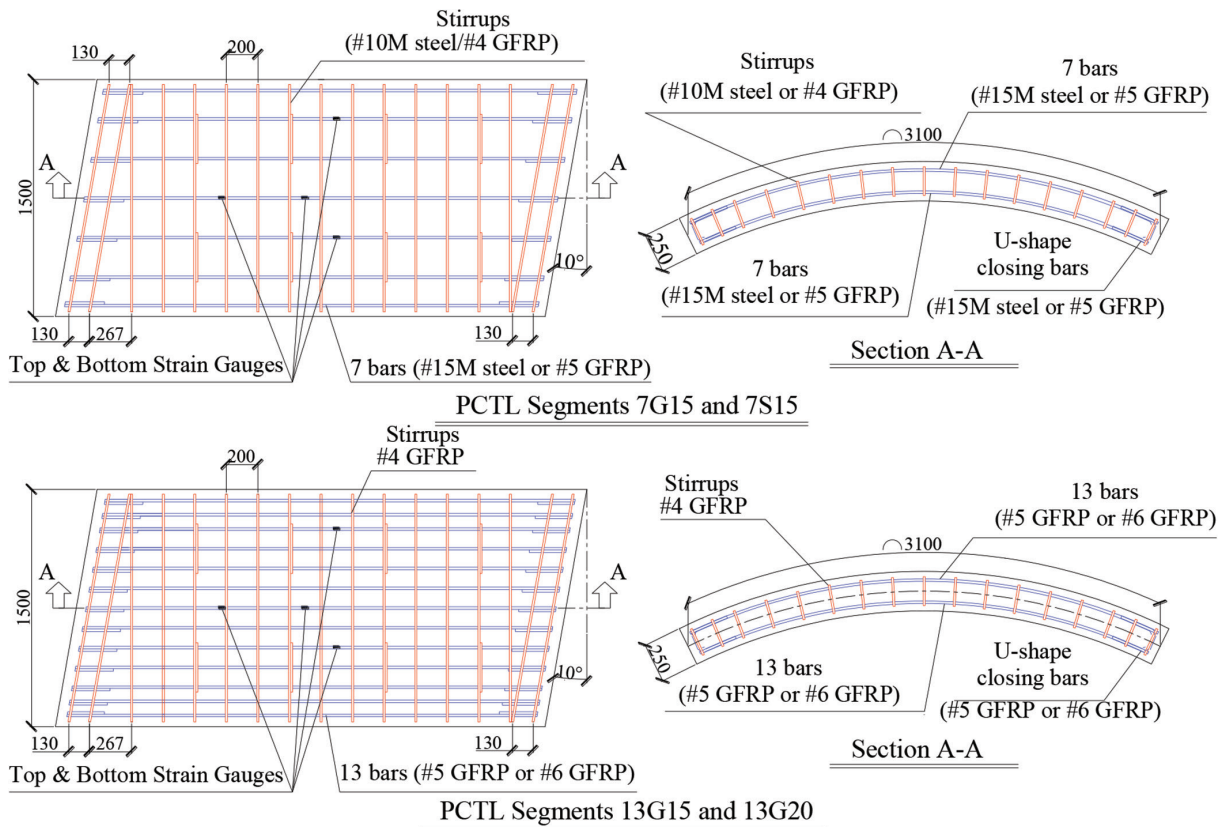


Fig. 2—Reinforcement details for test specimens. (Note: All dimensions in mm; 1 mm = 0.0394 in.)

No. 5 U-shaped GFRP anchorage bars were installed on each side of the specimen. Specimens 13G15 and 13G20 had top and bottom longitudinal reinforcement consisting of 13 No. 5 GFRP bars and 13 No. 6 GFRP bars with longitudinal reinforcement ratios of 0.9% and 1.25%, respectively. Thirteen No. 5 U-shaped GFRP anchorage bars and 13 No. 6 U-shaped GFRP anchorage bars were installed on each side of Specimens 13G15 and 13G20, respectively. All the GFRP specimens were reinforced transversally with No. 4 GFRP ties at a spacing of 200 mm (7.87 in.). The control steel specimen (7S15) had top and bottom longitudinal reinforcement consisting of seven M15 deformed steel bars with a reinforcement ratio of 0.5% and transverse reinforcement consisting of M10 ties at a spacing of 200 mm (7.87 in.). Seven deformed 15M U-shaped anchorage steel bars were installed on each side of the specimen. Figure 2 shows the reinforcement details for all the test specimens. The clear cover was kept constant at 40 mm (1.57 in.) for all specimens.

Instrumentation and test setup

Strains in the longitudinal and transverse reinforcing bars were measured with electrical resistance strain gauges with a gauge length of 10 mm (0.39 in.) (Fig. 2). In addition, five strain gauges with a gauge length of 60 mm (2.36 in.) were mounted on the concrete surface at the mid- and quarter span to measure the concrete compressive strain. Specimen deflections were measured with five linear potentiometers (LPOTs) placed at the mid- and quarter span. The test setup was designed and fabricated at the University of Sherbrooke's CFI structural laboratory.

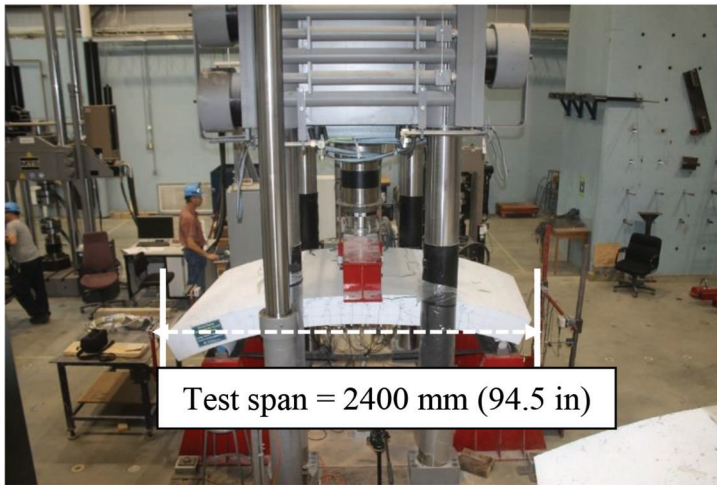
The specimens were loaded under three-point bending load, as shown in Fig. 3(a), using an 11,000 kN (247.3 kip) capacity universal testing machine attached to a spreader beam. The span for the test specimens was 2400 mm (94.5 in.). The load was applied at a displacement-controlled rate of 0.8 mm/min. An automatic data-acquisition system monitored by a computer was used to record the readings of the LPOTs, load cells, and strain gauges.

Quasi-static cyclic loading procedure

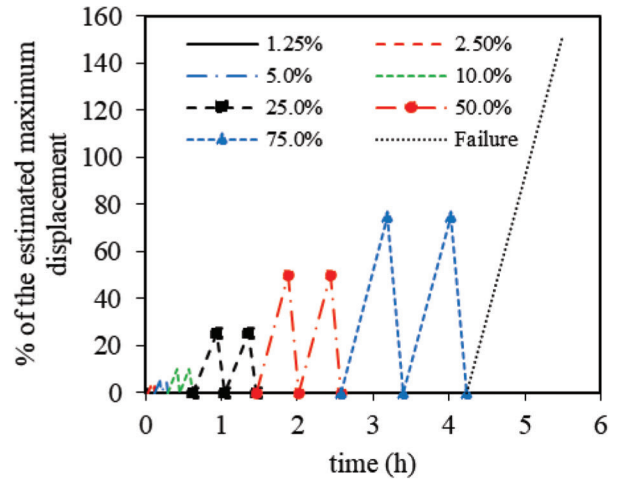
The test protocol followed is that in ACI 374.2R-13: tests of structural components under slowly applied quasi-static loading, either as monotonically increasing or reversed cyclic loading. Quasi-static cyclic flexural loading was applied in terms of the percentage of the maximum displacement (Δ_{max}) obtained from the static testing results in the literature (Hosseini et al. 2022). Two cycles of loading and unloading were conducted for 1.25, 2.5, 5, 10, 25, 50, and 75% of Δ_{max} , followed by one cycle up to failure. In all cycles, the unloading phase was finished with a minimum load of 5 kN (1.12 kip) to keep the test jack engaged. Figure 3(b) shows the loading scheme for the tested specimens.

TEST RESULTS AND DISCUSSION

This section summarizes the experimental results, including the general behavior of the test specimens in terms of hysteresis response, crack patterns and failure modes, strain in reinforcement and concrete, neutral-axis depth, deformability, dissipated energy, and ductility and secant-stiffness damage index. Table 3 summarizes the



(a)



(b)

Fig. 3—(a) Test setup; and (b) loading scheme for tested specimens.

Table 3—Summary of experimental and theoretical results

Specimen ID	Cracking moment, kN·m	Failure moment, kN·m	M_{exp}/M_{pred}					V_{exp}/V_{pred}				
			ACI 440.1R-15	CSA S806-12	fib TG-9.3-2007	AFGC 2021	CNR-DT 203-2006	ACI 440.1R-15	CSA S806-12	fib TG-9.3-2007	AFGC 2021	CNR-DT 203-2006
7G15	48	206	0.97	0.86	0.96	0.96	1.29	1.63	1.11	1.26	1.19	0.81
13G15	49	243*	0.87	0.78	0.81	0.87	0.88	1.44	1.09	1.11	1.14	0.85
13G20	55	238†	0.76	0.68	0.68	0.77	0.67	1.28	0.97	0.99	1.01	0.76

*Shear load failure = 178 kN (40.02 kip).

†Shear load failure = 174 kN (39.12 kip).

Note: 1 mm = 0.0394 in.; 1 kN·m = 0.738 kip·ft.

flexural moment and shear load-carrying capacities of the test specimens.

Hysteresis response

The hysteresis behavior is shown in the form of the moment versus midspan deflection of specimens, as presented in Fig. 4. Initially, all the specimens exhibited identical linear load-deflection behavior. After cracking, the stiffness of the GFRP specimens reduced with almost linear load-deflection behavior. The steel-reinforced specimen also had initial linear load-deflection behavior corresponding to the uncracked condition of the specimen. Its stiffness decreased due to yielding of the longitudinal reinforcement in the tension zone, followed by a gradual decrease in overall stiffness. Figure 5 shows the cracking pattern in the test specimens. The first vertical flexural crack initiated in the tension zone under the loading point. The corresponding cracking moment was recorded during testing and verified from the moment-strain and moment-deflection relationships. The cracking moment M_{cr} ranged from 48 to 55 kN·m (35.40 to 40.57 kip·ft), occurring in the first cycle at 5% of the maximum displacement. At this stage, there were no significant strain-gauge readings for the GFRP or steel reinforcing bars before initiation of the first flexural crack. In addition, the concrete strains were insignificant in all specimens, ranging from -60 to $-130 \mu\epsilon$ at the top location

of the midspan, as shown in Fig. 6(a). Beyond the first cracking load, additional flexural cracks developed within the shear span of the 7G15 specimen, in the 10% and 25% maximum displacement cycles. With further loading, in the first 75% of the maximum displacement cycle, the flexural cracks became wider and propagated upward towards the loading point, while some new cracks started to develop in the shear span (Fig. 5). Before failure occurred, the cracks along the shear span started to incline towards the loading points. The concrete crushing moment M_n for the 7G15 specimen was 206 kN·m (151.9 kip·ft), with a maximum recorded midspan concrete compressive strain of $-3840 \mu\epsilon$ on concrete crushing, as shown in Fig. 6(a). Specimens 13G15 and 13G20 behaved similarly before 75% of the maximum displacement cycle. Beyond this stage, a main shear crack started to develop and propagated until shear failure occurred at a shear load V_n of 178 and 174 kN (40.02 and 39.12 kip), respectively. The failure of Specimens 13G15 and 13G20 occurred by shear compression failure and diagonal tension failure, respectively. The maximum recorded midspan concrete compressive strain in specimen 13G15 was $-3285 \mu\epsilon$, indicating shear compression failure. In contrast, the diagonal tension failure in Specimen 13G20 resulted in a maximum midspan concrete compressive strain of $-2051 \mu\epsilon$, as shown in Fig. 6(a). The hysteretic response for the GFRP-reinforced specimens, in all second excursion

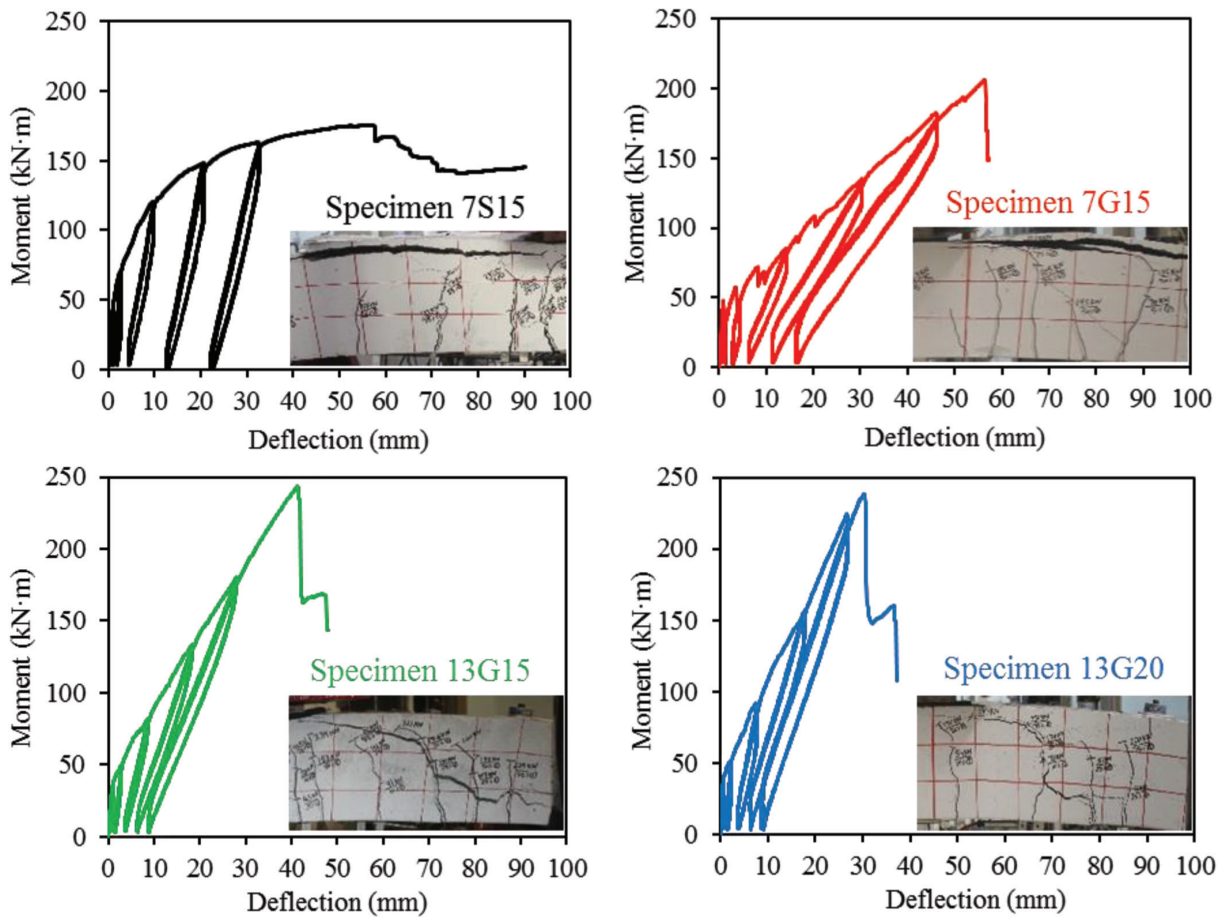


Fig. 4—Hysteresis response and failure mode of test specimens.

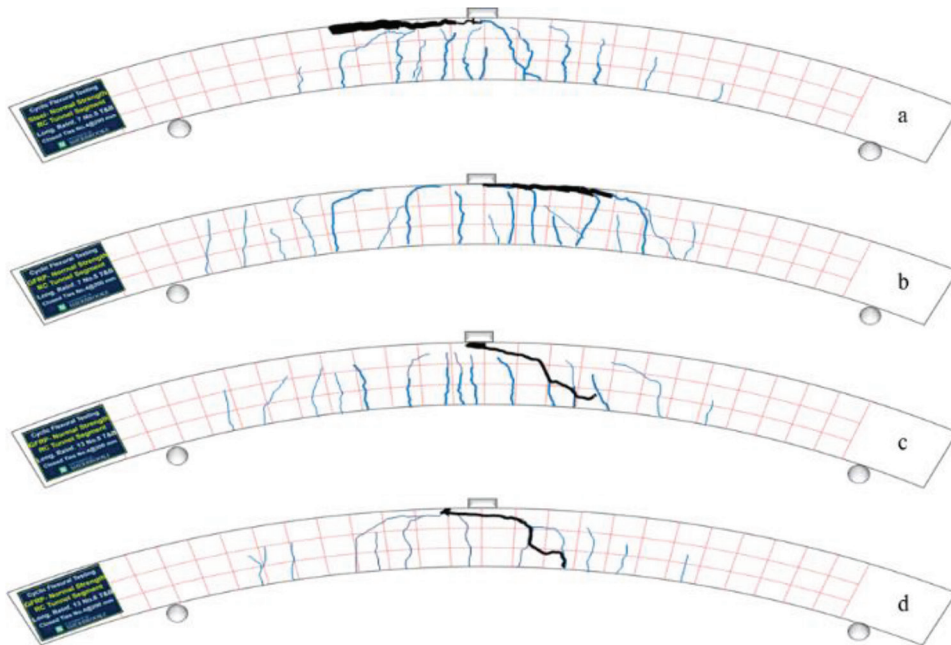


Fig. 5—Cracking pattern in: (a) Specimen 7S15; (b) Specimen 7G15; (c) Specimen 13G15; and (d) Specimen 13G20.

loading cycles, reflected stable cyclic behavior with no or limited strength degradation until failure. In contrast, the early yielding of the steel bars in specimen 7S15 resulted in wider concentrated cracks compared to the GFRP-reinforced specimens. Specimen 7S15 yielded (at a corresponding

strain of approximately $2300 \mu\epsilon$) in the first 25% of the maximum displacement cycle at an applied moment of $114 \text{ kN}\cdot\text{m}$ ($84.1 \text{ kip}\cdot\text{ft}$) (approximately at 64% of the specimen's peak moment). The midspan concrete compressive strain reading in Specimen 7S15 when the steel yielded was

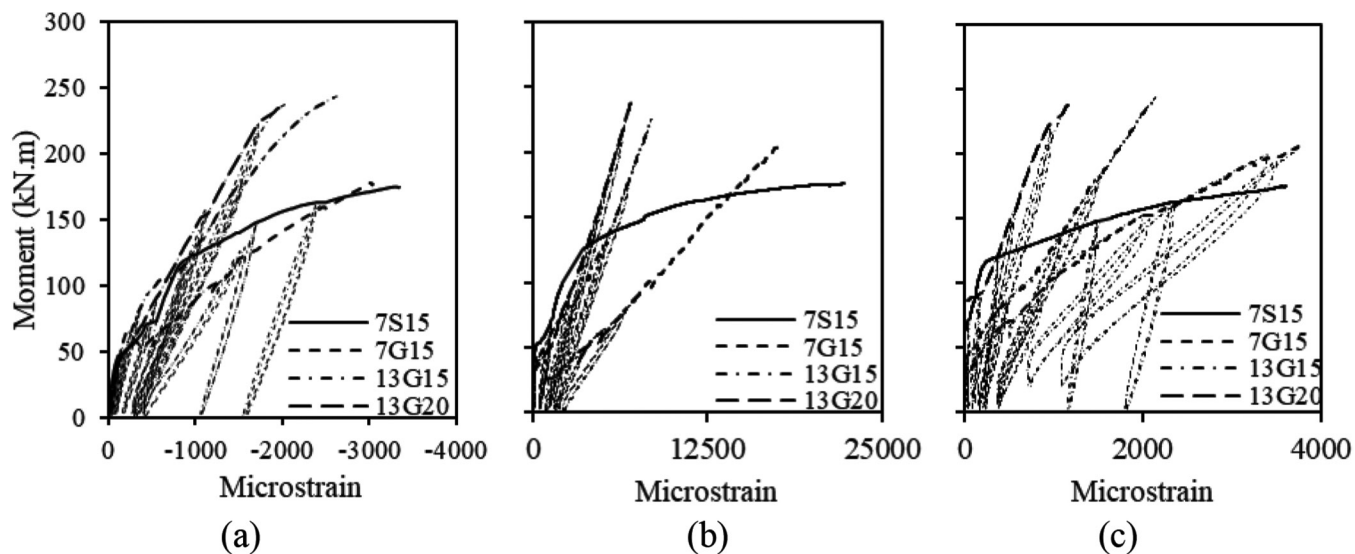


Fig. 6—Moment-strain relationship at midspan at: (a) concrete surface; (b) bottom reinforcement bars; and (c) top reinforcement bars.

–795 $\mu\epsilon$, as shown in Fig. 6(a). The concrete strain gauge continued recording after this point until the ultimate applied moment of 176 kN·m (129.8 kip·ft) (concrete crushing) at 3336 $\mu\epsilon$. The strain in the GFRP bars on the tension side gradually increased up to specimen failure at 17,695, 8508, and 7023 $\mu\epsilon$ (88%, 43%, and 35% of the ultimate tensile strain of the GFRP bars) for Specimens 7G15, 13G15 and 13G20, respectively, as shown in Fig. 6(b). In addition, the strain-gauge readings show that the top reinforcement bars in all the specimens were under tension, which enhanced specimen strength. The recorded strains in Specimens 7S15, 7G15, 13G15, and 13G20 in the top reinforcement (GFRP or steel bars) at failure were 3761, 2163, 1164, and 3603 $\mu\epsilon$, respectively, as shown in Fig. 6(c). The test results indicate that the recorded strains at the quarter span for both the reinforcement bars and the concrete surface were less than that at midspan.

Unloading stiffness and residual deformation

Unloading stiffness is an important parameter because it determines the value of the residual deformation, thus determining the recoverability of the structure (Fahmy et al. 2009). As shown in Fig. 4, the unloading stiffness for the GFRP-reinforced specimens in all cycles was nearly equal to the reloading stiffness. In contrast, the yielding of the steel bars in Specimen 7S15 at 25% of the maximum displacement cycle resulted in higher residual deformation compared to the GFRP-reinforced Specimen 7G15. The average unloading stiffness of Specimen 7S15 at 25%, 50%, and 75% of the estimated maximum displacement cycles was 95%, 85%, and 89%, respectively, of the reloading stiffness. Residual deformation is often used as a key measure of the required recoverability of RC structures (Dong et al. 2016). Figure 7 compares the cumulative residual deformation of Specimens 7G15 and 7S15. The residual deformation of the GFRP-reinforced specimen during unloading at 50% and 75% of the maximum displacement cycles was less than that of the steel-reinforced specimen due to the yielding

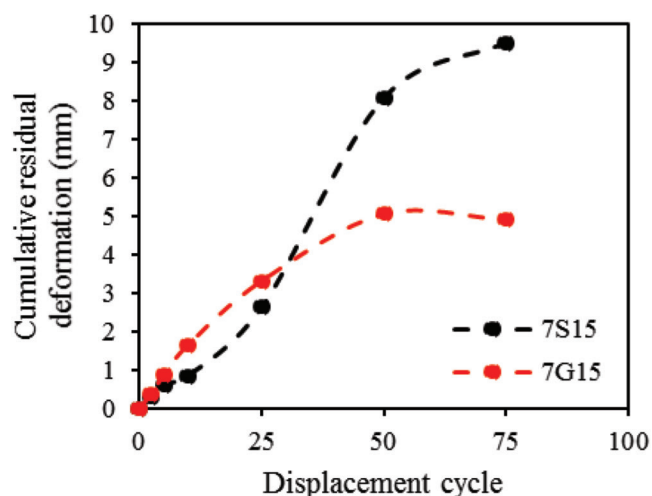
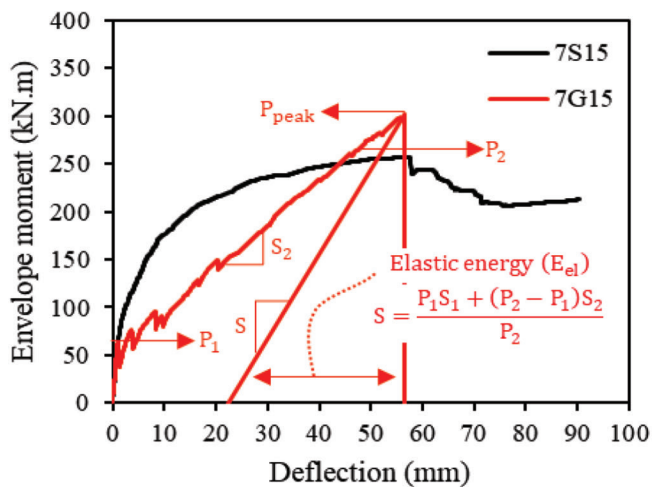


Fig. 7—Cumulative residual deformation for GFRP-reinforced (7G15) versus steel-reinforced (7S15) specimens with similar reinforcement ratios.

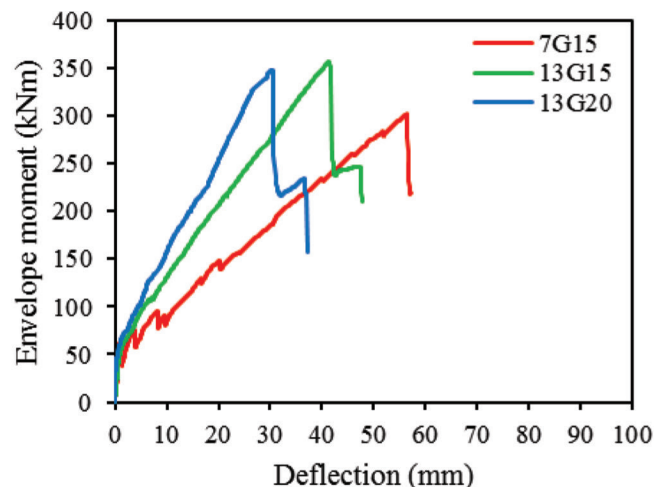
of the steel bars in the tension zone. In general, the GFRP specimens recovered most of their deflection during the unloading at 50% and 75% of the maximum displacement cycles. When 50% of the maximum displacement cycles in Specimen 7S15 was exceeded, a permanent deflection occurred in the unloading cycles due to the yielding of the steel bars.

Effect of parameters

This section presents the envelope moment-deflection curves at the midspan of the test specimens in two groups to show the effect of test parameters on specimen behavior, as depicted in Fig. 8. Before cracking occurred, identical linear moment-deflection behavior was observed in all the test specimens, regardless of reinforcement ratio and type, representing the uncracked condition governed by the properties of the concrete section. After cracking occurred, the response of the GFRP-reinforced specimens was almost linear up to failure. The moment-deflection curve of the



(a)



(b)

Fig. 8—Effect of test parameters on envelope moment-deflection relationship: (a) stiffness of longitudinal reinforcement; and (b) longitudinal reinforcement ratio.

steel-reinforced specimen shows a typical yielding plateau, followed by concrete crushing in the compression zone. Afterward, a sudden load drop occurred, followed by total loss of flexural stiffness.

Effect of axial stiffness of longitudinal reinforcement

Specimens 7G15 and 7S15 were designed to have the same flexural longitudinal reinforcement ratio. Before Specimen 7G15 cracked, its stiffness was similar to that of 7S15, as shown in Fig. 8(a). Specimen 7G15 had lower post-cracking flexural stiffness—calculated as the average slope of the curve—than its steel-reinforced counterpart (Specimen 7S15). The ratio between the post-cracking flexural stiffness of Specimens 7S15 to 7G15 was approximately 4.28. This ratio is approximately the same as the 4.35 ratio of the axial stiffness (EA) of the steel to that of the GFRP bars. This is in good agreement with the results of Mousa et al. (2018). It can be seen, however, that the GFRP-reinforced specimen had a longer ascending branch with higher stiffness compared to the post-yielding flexural stiffness of the steel-reinforced specimen. This is mainly due to the fact that, after the steel bars yielded, their tangent modulus was lower than that of the GFRP bars, which maintained their modulus of elasticity throughout the entire duration of loading. In addition, the test results indicate that Specimen 7G15 had 1.5 times the flexural strength of Specimen 7S15 at yielding, as shown in Table 3. The higher strength gain of the GFRP specimen provided sufficient deformability according to the CSA S6-19 (2019) code limit of 4 for rectangular sections, so that warning of failure in the form of excessive deflection and cracking would be expected before reaching the GFRP bars reached their rupture tensile strain.

Effect of longitudinal reinforcement ratio

The three GFRP-reinforced specimens (7G15, 13G15, and 13G20) were designed to have reinforcement ratios of 0.50%, 0.90%, and 1.20%, respectively. Figure 8(b) provides a comparison of the envelope moment-deflection curves for

the three specimens, indicating that Specimen 13G15 had ultimate strength 18% higher than Specimen 7G15, as shown in Table 3. Moreover, Table 3 shows that the percentage was lower when comparing Specimen 13G20 to 13G15. This could be attributed to the fact that the failures of Specimens 13G15 and 13G20 were shear compression failure and diagonal tension failure, respectively. The post-cracking flexural stiffness of Specimen 13G15 (reinforcement ratio of 0.90%) was 72% higher than that of Specimen 7G15 (reinforcement ratio of 0.50%). Similarly, the post-cracking flexural stiffness of Specimen 13G20 (reinforcement ratio of 1.20%) was 140% higher than that of Specimen 7G15 (reinforcement ratio of 0.50%) and 39% higher than that of Specimen 13G15 (reinforcement ratio of 0.90%). These percentages were approximately similar to the percentage increases in the reinforcement ratios (80% from 0.50 to 0.90%, 33% from 0.90 to 1.2%, and 140% from 0.50 to 1.2%).

Strain distribution over cross section

An analysis of strains along the cross section was carried out using the results from the concrete and bar strain gauges at the midspan of the specimens; the experimental neutral-axis depth was deduced. Figure 9 presents the strain profile along the depth of the section at different moment levels. The figure shows a linear strain profile with some deviation. It is worth mentioning, however, that the strain gauges in Specimen 13G15 were damaged before failure because several cracks occurred in the instrumented region. The Bernoulli hypothesis (a plane section remains plane after deformation up to failure), however, could be considered an acceptable simplification of this behavior. Figure 10 illustrates the relation between neutral-axis depth at midspan with the applied moment for the test specimens. In all test specimens, the position of the neutral axis in a section prior to cracking remained unchanged at the geometrical centroid of the specimen cross section. After cracking occurred, the neutral axis depth decreased rapidly at first and then tended to stabilize. In the GFRP-reinforced specimens, the stabilizing behavior continued up to concrete crushing. In contrast, the yielding

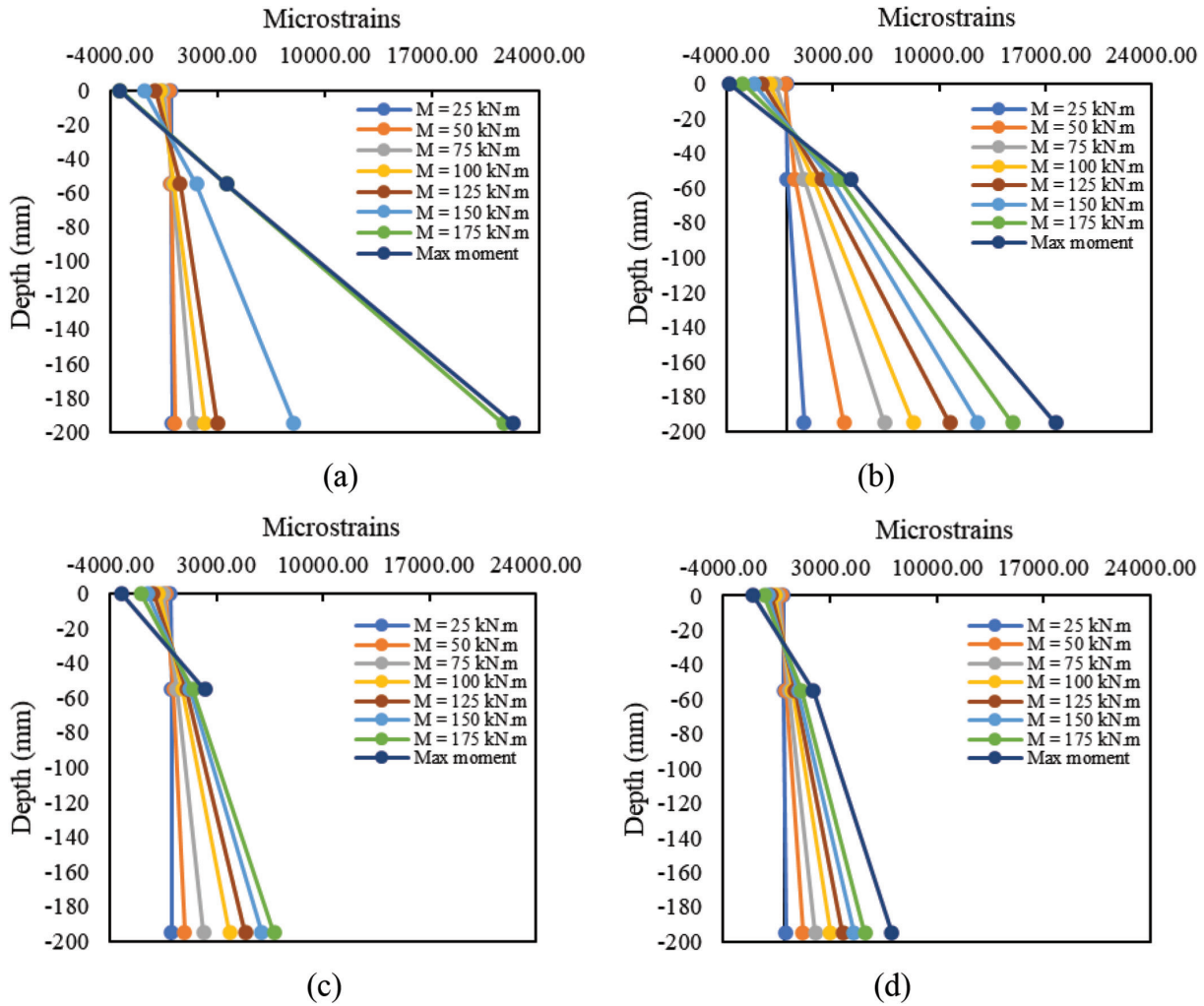


Fig. 9—Strain along midspan section for Specimens: (a) 7S15; (b) 7G15; (c) 13G15; and (d) 13G20.

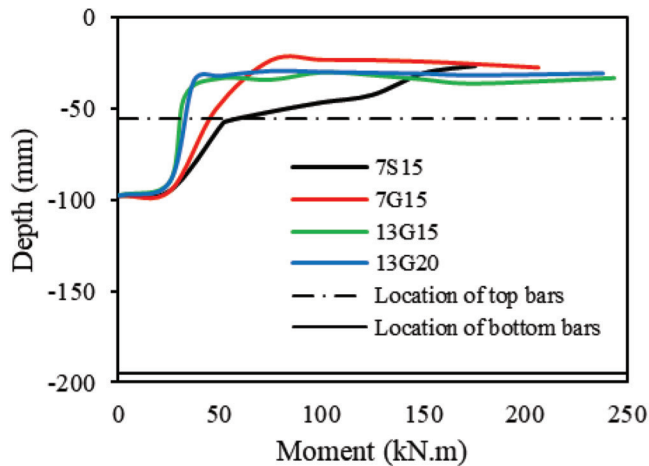


Fig. 10—Neutral-axis depth.

of tensile steel in the reinforced-steel specimen resulted in a rapid decrease in the neutral axis depth. Figure 10 also shows that the neutral-axis depth for Specimen 7G15 was less than that of Specimen 7S15 despite them having similar reinforcement ratios. This could be attributed to the difference in the modulus of elasticity of the GFRP and steel bars.

Cumulative dissipated energy

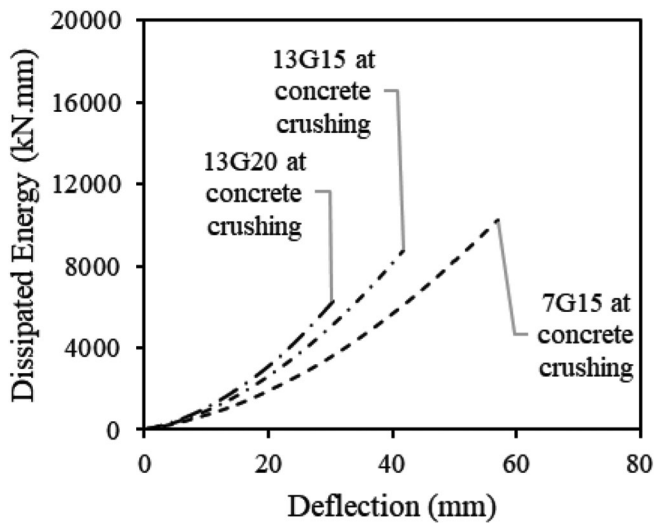
Earthquakes transfer energy into structures that must then be dissipated for safety reasons. The measurement of dissipated energy could thus become a good efficiency index independently of structural ductility considerations. During cyclic tests on structures, dissipative mechanisms are frequently encountered and must be distinguished to determine the action of reinforcement on the dissipated energy (Eq. (1)). In fact, a principal energy E_T is transferred to the structure and supports. One component of this energy is redistributed into the soil E_S , while the other is used by the structure over the elastic E_e and inelastic E_a domains. The first component E_e represents the energy necessary both for specimen displacement (kinematic energy E_c) and for elastic strain E_{es} . The component E_a includes the damping energy E_d and hysteretic energy E_h (Daniel and Loukili 2002).

$$E_T - E_S = E_e + E_a \quad (1)$$

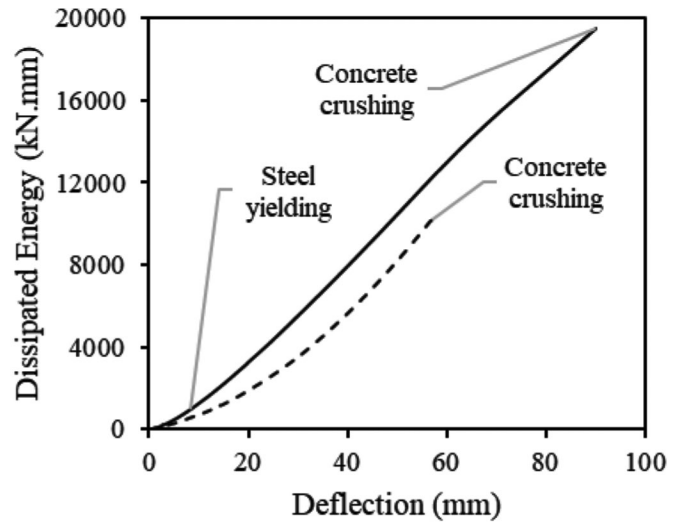
$$E_e = E_c + E_{es} \quad (2)$$

$$E_a = E_d + E_h \quad (3)$$

To avoid structural collapse from occurring, it is important to increase the energy storage capability in the elastic



(a)



(b)

Fig. 11—Dissipated energy versus normalized deflection for: (a) specimens with different longitudinal reinforcement ratios; and (b) specimens with different reinforcement type.

domain and energy dissipation in the inelastic domain. For the former, increasing the longitudinal reinforcement ratio increases structural stiffness. Therefore, having higher reinforcement ratio prevents increasing energy storage in the inelastic domain, as shown in Fig. 11(a). The computation of primary dissipated energy was carried out up until concrete crushing. The energy dissipated during a loading cycle was determined by computing the hysteretic area of the loop. The overall dissipated energy of Specimen 7G15 was 16% and 63% higher than that of Specimens 13G15 and 13G20, respectively. Similarly, the overall dissipated energy of Specimen 13G15 was 40% higher than that of Specimen 13G20. Considering the type of reinforcement, Fig. 11(b) shows that Specimen 7G15, at concrete crushing failure, showed approximately 10 times the cumulative dissipated energy than its steel-reinforced counterpart Specimen 7S15, at steel yielding. The steel specimen's cumulative dissipated energy, however, was approximately twice the cumulative dissipated energy of GFRP-reinforced Specimen 7G15 at concrete crushing.

Energy-based ductility index

Ductility is a structural-design requirement in most design codes. The traditional definition of ductility for steel-reinforced concrete members, which considers the yielding of steel bars as a reference point, cannot be directly applied to members reinforced with FRP reinforcement due to the linear elastic behavior of FRP bars up to failure. Several methods have been proposed to calculate the ductility of FRP-RC structures. Naaman and Jeong (1995) defined ductility as the ratio of the total energy to the elastic energy and proposed Eq. (4) to compute the ductility index μ_e , which can be applied to steel- and FRP-reinforced concrete members

$$\mu_e = 0.5((E_{tot}/E_{el}) + 1) \quad (4)$$

where E_{tot} is the total energy computed as the area under the load-deflection curve; and E_{el} is the elastic energy released upon failure, computed as the area of the triangle formed at failure load by the line having the weighted average slope of the two initial straight lines of the load-deflection curve, as illustrated in Fig. 8(a). The computed energy-based ductility index μ_e for Specimens 7G15, 13G15, 13G20, and 7S15 were 1.5, 1.3, 1.3, and 1.9, respectively. Considering the type of reinforcement, Specimen 7G15 had a ductility index equal to 78% of the ductility of Specimen 7S15, its steel-reinforced counterpart. This difference in ductility was compensated for by the high strength reserve of Specimen 7G15, which had flexural strength 150% higher than Specimen 7S15 at yielding. Moreover, the computed μ_e was slightly lower when the reinforcement ratio was increased. In the case of Specimen 13G15, increasing its reinforcement ratio resulted in a computed μ_e slightly lower than that of Specimen 7G15 (from 1.5 to 1.3). Further increasing the reinforcement ratio did not lower the computed μ_e for Specimen 13G20 further.

Deformability factor

ACI 440.1R-15 defines the deformability factor as the ratio of the energy absorption at ultimate strength of the section to the energy absorption at the service level. The Canadian Highway Bridge Design Code (CSA S6-19) adopted the Jaeger et al. (1997) (J-factor) approach to evaluate the deformability index of FRP-RC members. The J-factor takes into account the strength effect as well as the curvature effect at service and ultimate conditions. Equation (5) can be used to calculate the deformability J-factor

$$J = \frac{M_{ultimate}}{M_s} \times \frac{\Psi_{ultimate}}{\Psi_s} = \frac{M_{ultimate} \cdot \Psi_{ultimate}}{M_s \cdot \Psi_s} \quad (5)$$

where Ψ_s is the curvature at service condition (concrete strain equal to 0.001); Ψ_u is the curvature at ultimate; M_s is the moment at service condition; and M_u is the ultimate moment. CSA S6-19 requires a J-factor greater than 4 for

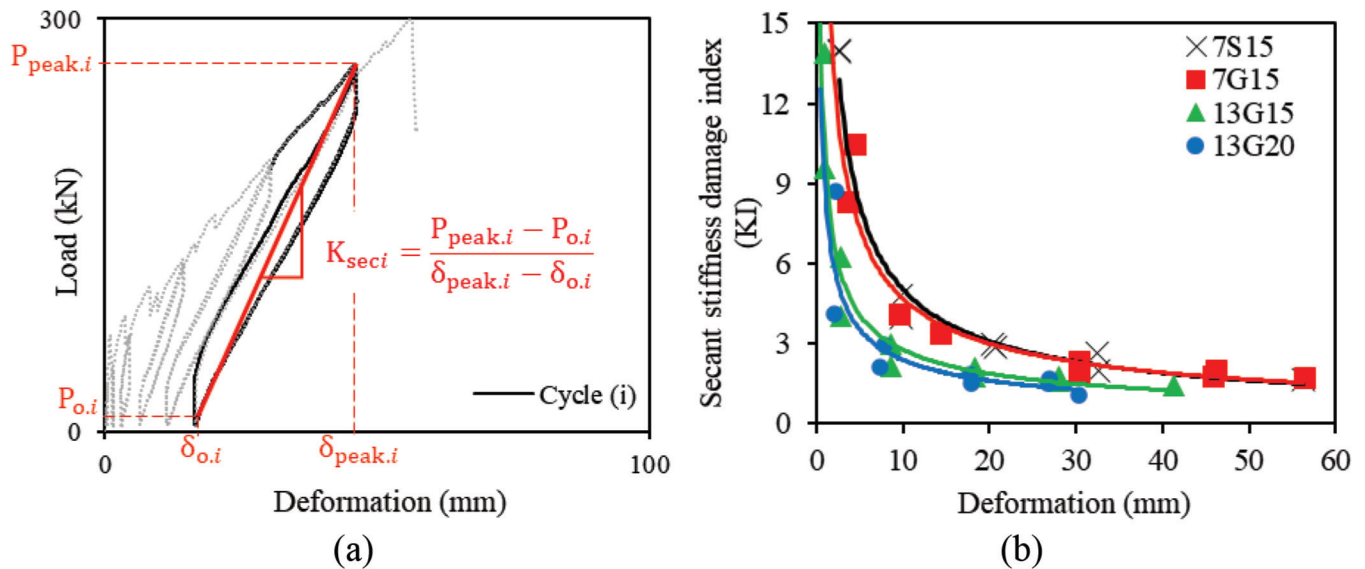


Fig. 12—(a) Secant stiffness; and (b) secant stiffness damage index versus deflection.

rectangular sections: the higher the J-factor values, the more sufficient warning given by the FRP-RC specimen before failure. In other words, the J-factor indicates the amount of cracking and deflection that the FRP-RC member will exhibit throughout the load history from service to ultimate condition. The computed deformability J-factor shows that all the GFRP-reinforced specimens demonstrated adequate deformability when compared to the CSA S6-19 code limit of 4 for rectangular sections. The deformability J-factors for Specimens 7G15, 13G15, and 13G20 were 7.1, 6.1, and 4.1, respectively.

Secant-stiffness damage index

Several researchers have established a set of damage indexes to ascertain the residual capacity of structures (Daniel and Loukili 2002; Ranjbaran et al. 2018). A wide array of parameters may be used, such as number of cycles, stiffness, and ductility. This section discusses the effect of the longitudinal reinforcement ratio on the secant stiffness index (KI) in loading and unloading. The parameter's values and changes are the index of damage in the specimens. This stiffness index is described as the cycle's secant stiffness K_{seci} to the after-cracking stiffness ratio of the specimens. For each loading cycle, the cycle's secant stiffness damage index K_{seci} was computed using Eq. (6), as illustrated in Fig. 12(a).

$$K_{seci} = \frac{P_{peak,i} - P_{o,i}}{\delta_{peak,i} - \delta_{o,i}} \quad (6)$$

Figure 12(b) illustrates the effect of the GFRP longitudinal reinforcement ratio on the secant stiffness damage index (KI). As shown, GFRP-reinforced PCLT Specimen 7G15 had a decrease in stiffness comparable to that of its counterpart Specimen 7S15. Moreover, increasing the longitudinal reinforcement ratio did not significantly affect the rate of decrease in stiffness. The residual stiffness at ultimate deflection of Specimen 13G15 (reinforcement ratio of 0.90%) was 18.8% lower than that of Specimen 7G15 (reinforcement ratio of 0.50%). Similarly, the residual stiffness at ultimate deflection of Specimen 13G20 (reinforcement ratio

of 1.20%) was 34.9% lower than that of Specimen 13G15 (reinforcement ratio of 0.90%).

THEORETICAL STUDY

This section presents a theoretical study to calculate the flexural and shear capacities of PCTL segments reinforced with GFRP bars. It provides the calculations of the flexural and shear capacities of the PCTL tunnel segments reinforced with GFRP bars considering the requirements in ACI 440.1R-15, CSA S806-12(R2017), *fib* TG-9.3, CNR-DT 203, and AFGC.

Flexural capacity

The flexural design of FRP-reinforced concrete members is analogous to the design of steel-reinforced concrete members. Experimental data on concrete members reinforced with FRP bars show that the flexural capacity can be calculated based on assumptions similar to those made for members reinforced with steel bars (Ruan et al. 2020). The flexural strength of the FRP-reinforced cross section is calculated based on the following assumptions:

- Strain in the concrete and the FRP reinforcement is proportional to the distance from the neutral axis (a plane section before loading remains plane after loading).
 - The tensile strength of the concrete is ignored.
 - The tensile behavior of the FRP reinforcement is linearly elastic until failure.
 - A perfect bond exists between the concrete and FRP reinforcement.
 - The maximum usable compressive strain in the concrete is assumed to be 0.003 in ACI 440.15 and 0.0035 in CSA S806-12, *fib* TG-9.3, CNR-DT 203, and AFGC.
- ACI 440.1R (2015)—The FRP reinforcement ratio is computed according to ACI 440.1R-15 with Eq. (7), and the balanced FRP reinforcement ratio can be computed with Eq. (8)

$$\rho_f = A_f/bd \quad (7)$$

where A_f is the area of the FRP reinforcement; b is the width of the rectangular cross section; and d is the distance from the extreme compression fiber to the centroid of the tension reinforcement

$$\rho_{fb} = 0.85 \beta_1 \frac{f'_c}{f_{fu}} \frac{E_f \varepsilon_{cu}}{E_f \varepsilon_{cu} + f_{fu}} \quad (8)$$

where f'_c is the specified compressive strength of the concrete; f_{fu} is the design tensile strength of the FRP, defined as the guaranteed tensile strength multiplied by the environmental reduction factor; E_f is the design or guaranteed modulus of elasticity of FRP, defined as the mean modulus of a sample from the test specimens; and ε_{cu} is the ultimate strain in the concrete.

According to ACI 440.1R-15, when $\rho_f > \rho_{fb}$, the controlling limit state is crushing of the concrete, and the stress distribution in the concrete can be approximated with the ACI rectangular stress block. Based on the equilibrium of forces and strain compatibility, the following can be derived

$$M_n = A_f f_f (d - (a/2)) \quad (9)$$

$$a = \frac{A_f f_f}{0.85 f'_c b} \quad (10)$$

$$f_f = E_f \varepsilon_{cu} \frac{\beta_1 d - a}{a} \quad (11)$$

In ACI 440.1R-15, the nominal flexural strength is determined from Eq. (9) through (11).

The FRP reinforcement is linearly elastic at the concrete crushing limit state, so the stress level in the FRP can be found from Eq. (11), as it is less than f_{fu} .

Alternatively, the nominal flexural strength at a section can be expressed, according to ACI 440.1R-15, in terms of the FRP reinforcement ratio, as given in Eq. (12).

$$M_n = \rho_f f_f \left(1 - 0.59 \frac{\rho_f f_f}{f'_c} \right) b d^2 \quad (12)$$

CAN/CSA S806-12(R2017)—According to CAN/CSA S806-12(R2017), the concrete crushing mode of failure occurs in the FRP-reinforced section when the extreme compressive strain in the concrete reaches its ultimate strain, provided that

$$(c/d) \geq 7 / (7 + 2000 \varepsilon_{Fu}) \quad (13)$$

where c is the distance from the extreme compression fiber to the neutral axis; d is the distance from the extreme compression fiber to the centroid of the longitudinal tension force; and ε_{Fu} is the ultimate strain in the FRP reinforcement.

When c/d satisfies the requirements of Eq. (13), the nominal flexural strength in a section can be determined, similar to as in ACI 440.1R-15, based on the equilibrium of forces and strain compatibility.

fib TG-9.3 (2007)—According to fib TG-9.3, the ultimate flexural moment resistance of an FRP RC section can be evaluated by adopting the framework of Eurocode 2 (CEN 2004). Similar to as in ACI 440.1R-15, when $\rho_f > \rho_{fb}$, flexural

failure is expected to occur due to concrete crushing, and the ultimate moment resistance can be calculated based on the equilibrium of forces and strain compatibility with Eq. (14)

$$M_u = \eta f_{cd} b d^2 (\lambda \zeta) (1 - (\lambda \zeta / 2)) \quad (14)$$

where η is a factor defining the effective strength of the concrete; f_{cd} is the design value of the concrete compressive strength; b is the width of the rectangular cross section; d is the effective depth of a cross section; λ is a factor defining the effective height of the compression zone; and ζ is a reduction factor coefficient.

AFGC (2021)—As in fib TG-9.3, the ultimate flexural moment resistance of an FRP-RC section can be evaluated according to AFGC by adopting the framework of Eurocode 2 (CEN 2004). According to AFGC (2021), the FRP reinforcement ratio can be computed with Eq. (15), and the balanced FRP reinforcement ratio can be computed with Eq. (16)

$$\rho_{PRF} = A_{PRF} / A_{c,red} \quad (15)$$

where A_{PRF} is the area of the longitudinal reinforcement composite bars; and $A_{c,red}$ is the reduced area of the concrete section

$$\rho_{PRF,b} = \frac{\eta f_{cd} \lambda x_u}{\varepsilon_{PRF,u,d} E_{PRF} d} = \frac{\eta f_{cd} \lambda}{f_{PRF,d}} = \frac{\varepsilon_{cu2}}{\varepsilon_{PRF,u,d} + \varepsilon_{cu2}} \quad (16)$$

where η is a factor defining the effective strength of the concrete; f_{cd} is the design value of the concrete compressive strength; λ is a factor defining the effective height of the compression zone; x_u is the position of the neutral axis corresponding to the concrete balanced section; $\varepsilon_{PRF,u,d}$ is the limit strain of the FRP reinforcement; E_{PRF} is the FRP modulus of elasticity; d is the effective depth of a cross section; $f_{PRF,d}$ is the design FRP stress; and ε_{cu2} is the ultimate concrete strain.

Similar to fib TG-9.3, when $\rho_f > \rho_{fb}$, flexural failure is expected to occur due to concrete crushing, and the ultimate moment resistance M_{Rd} in AFGC can be calculated, based on the equilibrium of forces and strain compatibility, with Eq. (17)

$$\begin{aligned} M_{Rd} &= A_{PRF} E_{PRF} \varepsilon_{PRF} \left(d - \frac{\lambda x}{2} \right) \\ &= \lambda x \eta f_{cd} b \left(d - \frac{\lambda x}{2} \right) \end{aligned} \quad (17)$$

where A_{PRF} is the area of the longitudinal reinforcement composite bars; E_{PRF} is the FRP modulus of elasticity; ε_{PRF} is the strain in the FRP reinforcement; d is the effective depth of a cross section; λ is a factor defining the effective height of the compression zone; x is the position of the neutral axis; and f_{cd} is the design value of the concrete compressive strength.

CNR-DT 203 (2006)—CNR-DT 203 assumes that flexural failure takes place when one of the following conditions is met:

(a) The maximum concrete compressive strain, as defined by the current building code, is reached.

(b) The maximum FRP tensile strain ε_{fd} is reached. This value is computed from the characteristic tensile strength ε_{fk} with Eq. (18)

$$\varepsilon_{fd} = 0.9\eta_a(\varepsilon_{fk}/\gamma_f) \quad (18)$$

where η_a is an environmental conversion factor; and γ_f is a material partial factor.

For both failure modes, the nominal flexural strength in a section can be determined based on the equilibrium of forces and strain compatibility.

Shear capacity

The shear design of FRP-reinforced concrete is similar to that of steel-reinforced concrete members. The different mechanical properties of FRP bars, however, affect shear strength and should be considered. GFRP bars have a relatively low modulus of elasticity compared to steel, low transverse shear resistance, and high tensile strength with no yielding point. In addition, the tensile strength of the bent portion of an FRP bar is significantly lower than that of the straight portion.

ACI 440.1R-15—The concrete shear capacity V_c of flexural members using FRP as the main reinforcement can be evaluated according to ACI 440.1R-15 based on Eq. (19)

$$V_c = \frac{2}{5}\sqrt{f'_c}b_w(kd) \quad (19)$$

where b_w is the width of the web; k is the ratio of the neutral-axis depth to the reinforcement depth; and d is the distance from the extreme compression fiber to the centroid of the tension reinforcement.

CAN/CSA S806—In CSA S806-12 (R2017), the concrete shear capacity V_c for sections having an effective depth not exceeding 300 mm (12 in.) and with no axial load action on them can be calculated using Eq. (20)

$$V_c = 0.05\lambda\phi_c k_m k_r (f'_c)^{1/3} b_w d_v \quad (20)$$

where λ is a factor to account the concrete density; ϕ_c is the resistance factor for concrete; k_m is a coefficient taking into account the effect of moment in the section on the shear strength; k_r is coefficient taking into account the effect of reinforcement rigidity on its shear strength; f'_c is the specified concrete compressive strength; b_w is the minimum effective web width; and d_v is the effective shear depth.

According to CSA S806-12 (R2017), however, V_c shall not be taken as greater than $0.22\phi_c\sqrt{f'_c}b_w d_v$ or less than $0.11\phi_c\sqrt{f'_c}b_w d_v$.

fib TG-9.3 (2007)—*fib* TG-9.3 presents and discusses various shear design recommendations to allow for the use of FRP reinforcement for the various design specifications available. Moreover, the modification in Eq. (21) has been proposed for the ACI shear equation to compensate for the unnecessary conservative shear prediction

$$V_{c,proposed} = V_{c,ACI} \left(\frac{E_{FRP}}{E_s} \phi_s \right)^{1/3} \quad (21)$$

where $\phi_s = \varepsilon_f/\varepsilon_y$ represents the ratio between the maximum strain allowed in the FRP reinforcement ε_f and the yield strain of the steel ε_y .

AFGC (2021)—The concrete shear capacity $V_{Rd,c}$ of flexural members with FRP as the main reinforcement is determined according to the Eurocode 2 (CEN 2004) equation, as shown in Eq. (22)

$$V_{Rd,PRF} = C_{Rd,c} k \left(100 \frac{E_{PRF}}{E_s} \cdot \frac{A_{PRF}}{b_w d} f_{ck} \right)^{1/3} b_w d \quad (22)$$

where $C_{Rd,c} = 0.18/\gamma_c$; $k = \min\{2.0; 1 + \sqrt{200/d}\}$; E_{PRF} is the FRP modulus of elasticity; E_s is the steel modulus of elasticity; A_{PRF} is the area of the longitudinal reinforcement composite bars; b_w is the width of the web; d is the distance from the extreme compression fiber to the centroid of the tension reinforcement; and f_{ck} is the concrete compressive strength.

CNR-DT 203 (2006)—In CNR-DT 203, the concrete shear capacity $V_{Rd,ct}$ of flexural members with FRP as the main reinforcement can be evaluated with Eq. (23)

$$V_{Rd,ct} = 1.3 \left(\frac{E_f}{E_s} \right)^{1/2} \tau_{Rd} k (1.2 + 40\rho_1) b d \quad (23)$$

where E_f and E_s are the Young's modulus of elasticity of the FRP and steel bars; τ_{Rd} is the design shear stress; k is a coefficient to be set as equal to 1 for members if more than 50% of the bottom reinforcement is interrupted, and $(1.6 - d) \geq 1$ if that is not the case; ρ_1 is the FRP reinforcement ratio; b is the width of rectangular cross section; and d is the effective depth of the cross section.

Comparison of theoretical to experimental results

The nominal flexural-moment and shear-load capacities of the test segments were compared to the theoretical predictions according to ACI 440.1R-15, CAN/CSA S806-12(R2017), *fib* TG-9.3, AFGC, and CNR-DT 203. In all the theoretical analyses, the concrete density factor, material resistance factor, and member safety factor were taken as equal to unity. Table 3 presents the experimental-to-predicted ratios for the flexural and shear capacities of the segments. As shown in Table 3, ACI 440.1R-15 yielded accurate predictions for the segments' moment carrying capacity, where the experimental-to-predicted ratio for the moment capacity of Specimen 7G15 was 0.97. The ACI 440.1R-15 shear predictions were, however, conservative with experimental-to-predicted ratios of 1.44 and 1.28 for 13G15 and 13G20, respectively. The ACI shear modification model proposed in *fib* TG-9.3 compensated for the unnecessary conservatism in the ACI shear predictions. The *fib* TG-9.3 shear predictions were in good agreement with the experimental shear results with experimental-to-predicted ratios of 1.11 and 0.99 for 13G15 and 13G20, respectively. Moreover, both *fib* TG-9.3 and AFGC (2021) produced accurate predictions for the segments' moment-carrying capacity, where the experimental-to-predicted ratio for the moment capacity of Specimen 7G15 was 0.96 according to both. Moreover, the AFGC shear predictions were in good

agreement with the experimental shear results with experimental-to-predicted ratios of 1.14 and 1.01 for 13G15 and 13G20, respectively.

Furthermore, Table 3 illustrates that CAN/CSA S806-12(R2017) accurately predicted the shear capacity of the test segments with experimental-to-predicted ratios of 1.09 and 0.97 for 13G15 and 13G20, respectively. CAN/CSA S806-12(R2017), however, overestimated the moment carrying capacity of 7G15, with an experimental-to-predicted ratio of 0.86. On the other hand, considering the maximum FRP strain limit ϵ_{fd} in CNR-DT 203 resulted in conservative predictions of the moment capacities of the test segments. CNR-DT 203 underestimated the moment-carrying capacity of 7G15 with an experimental-to-predicted ratio of 1.29. Conversely, CNR-DT 203 overestimated the shear capacity of the test segments with experimental-to-predicted ratios of 0.85 and 0.76 for 13G15 and 13G20, respectively. Table 3 illustrates that all the design codes properly predicted the shear failure over the flexural failure for Specimens 13G15 and 13G20 with experimental-to-predicted flexural moment capacities less than 1 and experimental-to-predicted shear load capacities greater than 1. In contrast, all the design codes, except CNR-DT 203, failed to correctly predict the flexural failure of Specimen 7G15. However, it predicted that the concrete flexural crushing failure would occur before the shear failure at an experimental-to-predicted flexural moment and shear load ratios of 1.29 and 0.81, respectively.

CONCLUSIONS

This paper reports on an experimental and theoretical investigation of the behavior of precast concrete tunnel lining (PCTL) segments reinforced with glass fiber-reinforced polymer (GFRP) bars under quasi-static cyclic flexural loading. Based on the experimental results and the theoretical study presented in this paper, the following conclusions can be drawn:

1. The failure of Specimen 7G15 occurred by concrete crushing, while Specimens 13G15 and 13G20 failed due to shear compression and diagonal shear, respectively. Specimen 7S15, which was reinforced with steel, failed due to steel yielding, followed by concrete crushing.

2. The hysteresis cycles of the GFRP-reinforced specimens reflected stable cyclic behavior with no or limited strength degradation that was less than that experienced by the steel-reinforced specimen.

3. The unloading stiffness for the GFRP-reinforced specimens in all cycles was nearly equal to the reloading stiffness. The yielding of the steel bars in the steel-reinforced specimen resulted in degradation of the specimen's unloading stiffness.

4. The residual deformation of the GFRP-reinforced specimens during unloading at 50 and 75% of the maximum displacement cycles was less than in the steel-reinforced specimen due to the steel bars yielding.

5. The GFRP-reinforced specimens' ductility index was 78% of the steel-reinforced specimens' ductility at a similar reinforcement ratio. This difference in ductility was compensated for by the high strength reserve of Specimen 7G15.

Specimen 7G15 achieved a flexural strength 1.5 times that of Specimen 7S15 at yielding.

6. The test results show that all the GFRP-reinforced specimens demonstrated adequate deformability when compared to the CSA S6-19 (2019) code limit of 4 for rectangular sections.

7. The experimental results indicate that the hysteresis cycles of the GFRP-reinforced specimens had stable cyclic behavior with no or limited strength degradation. In addition, these specimens demonstrated adequate strength, ductility index, and deformability limits.

8. The experimental-to-predicted ratio of the flexural-moment capacity of Specimen 7G15 indicates good predictions for ACI 440.1R-15, *fib* TG-9.3 (2007), and AFGC (2021), while CAN/CSA S806-12(R2017) overestimated its flexural-moment capacity. On the other hand, CNR-DT 203 (2006) yielded conservative predictions of its flexural-moment capacity.

9. ACI 440.1R-15 produced conservative shear-load predictions for the test specimens. Conversely, CNR-DT 203 (2006) overestimated the shear-load capacities for the test segments. The ACI shear modification model proposed in *fib* TG-9.3, AFGC, and CAN/CSA S806-12(R2017) yielded accurate predictions of the shear-load capacities for the test specimens.

10. The experimental results were the first of their kind on the applicability of using GFRP as internal reinforcement for PCTLs under quasi-static cyclic flexural loading. These experimental results can be considered in the forthcoming provisions of ACI codes for the use of GFRP as internal reinforcement for PCTL applications.

AUTHOR BIOS

Basil Ibrahim is a Doctoral Candidate in the Department of Civil and Building Engineering at the University of Sherbrooke, Sherbrooke, QC, Canada. He received his BSc and MSc in civil engineering from the Faculty of Engineering, University of Sharjah, Sharjah, UAE. His research interests include the use of fiber-reinforced polymers (FRPs) in reinforced concrete structures.

Salaheldin Mousa is a Postdoctoral Fellow in the Department of Civil and Building Engineering at the University of Sherbrooke, where he also received his PhD. He received his BSc and MSc from and is a Lecturer at the Faculty of Engineering at Shoubra, Benha University, Cairo, Egypt. His research interests include the use of FRPs in reinforced concrete structures.

Hamdy M. Mohamed is a Lecturer and Research Associate in the Department of Civil and Building Engineering at the University of Sherbrooke, where he received his PhD. He received his BSc and MSc from the Faculty of Engineering at Helwan University, Cairo, Egypt. His research interests include the use and field applications of FRPs in reinforced concrete structures.

Brahim Benmokrane, FACI, is Professor in the Department of Civil and Building Engineering at the University of Sherbrooke, Tier-1 Canada Research Chair Professor in Advanced Composite Materials for Civil Structures and Industrial Research Chair Professor in FRP Reinforcement for Concrete Infrastructure, and Director of the University of Sherbrooke Research Center on Structural FRP Composite Materials for Concrete Structures (CRUSMAC). He is a member of ACI Committees 435, Deflection of Building Concrete Structures, and 440, Fiber-Reinforced Polymer Reinforcement; member and past Co-Chair of ACI Subcommittee 440-K, FRP-Material Characteristics; and member of ACI Subcommittees 440-E, Professional Education; 440-F, FRP-Repair-Strengthening; 440-H, FRP-Reinforced Concrete; 440-I, FRP-Prestressed Concrete; and 440-L, FRP-Durability. His research interests include the development of FRP reinforcement for concrete structures and their durability, structural performance, and field applications.

ACKNOWLEDGMENTS

This research was conducted with funding from the Natural Sciences and Engineering Research Council of Canada (NSERC), Mathematics of Information Technology and Complex Systems (MITACS), the Fonds de recherche du Québec en nature et technologies (FRQ-NT), The Pole de Recherche et d'Innovation en Matériaux Avancés au Québec (PRIMA Québec), and the Tier-1 Canada Research Chair in Advanced Composite Materials for Civil Structures. The authors are grateful to the precast company (Sym-Tech Béton Préfabriqué, Sainte-Hyacinthe, QC, Canada) and to the GFRP bar manufacturer (Pultrall Inc., Thetford Mines, QC, Canada) for their effective involvement in this project, and to the technical staff of the structural lab in the Department of Civil Engineering at the University of Sherbrooke.

REFERENCES

- Abbas, S., 2014, "Structural and Durability Performance of Precast Segmental Tunnel Linings," doctoral dissertation, Western University, London, ON, Canada.
- ACI Committee 374, 2013, "Guide for Testing Reinforced Concrete Structural Elements under Slowly Applied Simulated Seismic Loads (ACI 374.2R-13)," American Concrete Institute, Farmington Hills, MI, 18 pp.
- ACI Committee 440, 2015, "Guide for the Design and Construction of Structural Concrete Reinforced with Fiber-Reinforced Polymer (FRP) Bars (ACI 440.1R-15)," American Concrete Institute, Farmington Hills, MI, 88 pp.
- ACI Committee 533, 2020, "Guide for Precast Concrete Tunnel Segments (ACI 533.5R-20)," American Concrete Institute, Farmington Hills, MI, 80 pp.
- ACI Committee 544, 2016, "Report on Design and Construction of Fiber-Reinforced Precast Concrete Tunnel Segments (ACI 544.7R-16)," American Concrete Institute, Farmington Hills, MI, 36 pp.
- AFGC, 2021, "Réparation et renforcement des structures en béton au moyen des matériaux composites," Bulletin scientifique et technique de l'Association Française de Génie Civil, Paris, France. (in French)
- ASTM D7205-21, 2021, "Standard Test Method for Tensile Properties of Fiber Reinforced Polymer Matrix Composite Bars," ASTM International, West Conshohocken, PA.
- CAN/CSA-S6-19, 2019, "Canadian Highway Bridge Design Code," CSA Group, Toronto, ON, Canada.
- CAN/CSA S806-12(R2017), 2017, "Design and Construction of Building Components with Fiber-Reinforced Polymers," CSA Group, Toronto, ON, Canada.
- Caratelli, A.; Meda, A.; Rinaldi, Z.; Spagnuolo, S.; and Maddaluno, G., 2017, "Optimization of GFRP Reinforcement in Precast Segments for Metro Tunnel Lining," *Composite Structures*, V. 181, pp. 336-346. doi: 10.1016/j.compstruct.2017.08.083
- CEN, 2004, "Eurocode 2, Design of Concrete Structures—Part 1-1: General Rules and Rules for Buildings." European Committee for Standardization, Brussels, Belgium.
- Cheong, Y. W.; Kwan, H. P.; and Hariyanto, A. D., 2005, "Quality Control in Precast Production: A Case Study on Tunnel Segment Manufacture," *Journal of Architecture and Built Environment*, V. 33, No. 2.
- CNR-DT 203, 2006, "Guide for the Design and Construction of Concrete Structures Reinforced with Fiber-Reinforced Polymer Bars," National Research Council, Rome, Italy.
- Daniel, L., and Loukili, A., 2002, "Behavior of High Strength Fiber-Reinforced Concrete Beams under Cyclic Loading," *ACI Structural Journal*, V. 99, No. 3, May-June, pp. 248-256.
- Davis, J. R., ed., 2000, *Corrosion: Understanding the Basics*, ASM International, The Materials Information Society, Materials Park, OH, 571 pp.
- Dong, Z.; Zhang, P.; Zhu, H.; Wu, G.; and Wu, Z., 2016, "Study on Stiffness and Recoverability of Fiber Reinforced Polymers-Reinforced Concrete (FRP-RC) Composite T-Beams with Prefabricated Basalt Fiber-Reinforced Polymers Shell," *Journal of Reinforced Plastics and Composites*, V. 35, No. 6, pp. 516-529. doi: 10.1177/0731684415618019
- Fahmy, M.; Wu, Z. S.; and Wu, G., 2009, "Seismic Performance Assessment of Damage-Controlled FRP-Retrofitted RC Bridge Columns Using Residual Deformations," *Journal of Composites for Construction*, ASCE, V. 13, No. 6, pp. 498-513. doi: 10.1061/(ASCE)CC.1943-5614.0000046
- fib Task Group 9.3, 2007, "FRP Reinforcement in RC Structures," Fédération Internationale de Béton, Lausanne, Switzerland, 157 pp.
- Gulikers, J., 2003, "Problems Encountered in the Detection of Reinforcement Corrosion in Concrete Tunnel Linings—Theoretical Considerations," *Materials and Corrosion*, V. 54, No. 6, pp. 454-459. doi: 10.1002/maco.200390097
- Hosseini, S. M.; Mousa, S.; Mohamed, H. M.; and Benmokrane, B., 2022, "Structural Behavior of Precast RC Tunnel Segments with GFRP Bars and Ties Under Bending Load," *ACI Structural Journal*, V. 119, No. 1, Jan., pp. 307-319.
- Jaeger, L. G.; Mufti, A. A.; and Tadros, G., 1997, "The Concept of the Overall Performance Factor in Rectangular-Section Reinforced Concrete Members," *Proceedings, 3rd International Symposium on Non-Metallic (FRP) Reinforcement for Concrete Structures, FRPRCS-3*, V. 2, Japan Concrete Institute, Tokyo, Japan, pp. 551-559.
- Manalo, A.; Maranan, G.; Benmokrane, B.; Cousin, P.; Alajarmeh, O.; Ferdous, W.; and Hota, G., 2020, "Comparative Durability of GFRP Composite Reinforcing Bars in Concrete and in Simulated Concrete Environments," *Cement and Concrete Composites*, V. 109, p. 103564. doi: 10.1016/j.cemconcomp.2020.103564
- Meda, A.; Rinaldi, Z.; Spagnuolo, S.; De Rivaz, B.; and Giamundo, N., 2019, "Hybrid Precast Tunnel Segments in Fiber Reinforced Concrete with Glass Fiber Reinforced Bars," *Tunnelling and Underground Space Technology*, V. 86, pp. 100-112. doi: 10.1016/j.tust.2019.01.016
- Mousa, S.; Mohamed, H. M.; and Benmokrane, B., 2018, "Flexural Strength and Design Analysis of Circular Reinforced Concrete Members with Glass Fiber-Reinforced Polymer Bars and Spirals," *ACI Structural Journal*, V. 115, No. 5, Sept., pp. 1353-1364. doi: 10.14359/51702282
- Naaman, A. E., and Jeong, S. M., 1995, "Structural Ductility of Concrete Beams Prestressed with FRP Tendons," *Proceedings, 2nd International RILEM Symposium on Non-Metallic (FRP) Reinforcement for Concrete Structures*, RILEM, Bagneux, France, pp. 379-386.
- Rancourt, A., 2016, "Analysis of the Costs of a Tunnel Drilled between Beauport and Lévis," Report, Géosys, 35 pp.
- Ranjbaran, F.; Rezayfar, O.; and Mirzababai, R., 2018, "Experimental Investigation of Steel Fiber-Reinforced Concrete Beams under Cyclic Loading," *International Journal of Advanced Structural Engineering*, V. 10, No. 1, pp. 49-60. doi: 10.1007/s40091-018-0177-1
- Ruan, X.; Lu, C.; Xu, K.; Xuan, G.; and Ni, M., 2020, "Flexural Behavior and Serviceability of Concrete Beams Hybrid-Reinforced with GFRP Bars and Steel Bars," *Composite Structures*, V. 235, p. 111772. doi: 10.1016/j.compstruct.2019.111772
- Spagnuolo, S.; Meda, A.; Rinaldi, Z.; and Nanni, A., 2017, "Precast Concrete Tunnel Segments with GFRP Reinforcement," *Journal of Composites for Construction*, ASCE, V. 21, No. 5, p. 04017020. doi: 10.1061/(ASCE)CC.1943-5614.0000803
- Whitmore, D. W., and Ball, J. C., 2004, "Corrosion Management," *Concrete International*, V. 26, No. 12, Dec., pp. 82-85.
- Zhiqiang, Z., and Mansoor, Y. A., 2013, "Evaluating the Strength of Corroded Tunnel Lining Under Limiting Corrosion Conditions," *Tunnelling and Underground Space Technology*, V. 38, pp. 464-475. doi: 10.1016/j.tust.2013.08.003

aci[®] in Your Classroom

Integrate aci[®] into your classroom!

To support future leaders, ACI has launched several initiatives to engage students in the Institute's activities and programs – select programs that may be of interest to Educators are:

- **Free student membership** – encourage students to sign up
- **Special student discounts on ACI 318 Building Code Requirements for Structural Concrete, ACI 530 Building Code Requirements and Specification for Masonry Structure, & Formwork for Concrete manual.**
- **Access to Concrete International** – free to all ACI student members
- **Access to ACI Structural Journal and ACI Materials Journal** – free to all ACI student members
- **Free sustainability resources** – free copies of Sustainable Concrete Guides provided to universities for use in the classroom
- **Student competitions** – participate in ACI's written and/or team-based competitions
- **Scholarships and fellowships** – students who win awards are provided up to \$15,000 and may be offered internships and paid travel to attend ACI's conventions
- **ACI Award for University Student Activities** – receive local and international recognition for your University's participation in concrete-related activities
- **Free access to the ACI Collection of Concrete Codes, Specifications, and Practices** – in conjunction with ACI's chapters, students are provided free access to the online ACI Collection
- **ACI online recorded web sessions and continuing education programs** – online learning tools ideal for use as quizzes or in-class study material